Deciphering controls for the impact of geophysical flows on a flexible barrier: Insights from coupled CFD-DEM modeling

Yong Kong[1], and *Mingfu* Guan[1*]

[1]Department of Civil Engineering, The University of Hong Kong, Hong Kong, SAR, China.

Abstract. Geophysical flows impacting a flexible barrier can create complex flows and solid-fluid-structure interactions, which are challenging to quantify and characterize towards a unified description. Here, we examine the common physical laws of multiphase, multiway interactions during debris flows, debris avalanches and rock avalanches against a flexible barrier system using a coupled computational fluid dynamics and discrete element (CFD-DEM) method. This model captures essential physics observed in experiments and fields. The bi-linear, positive correlations are found between peak impact load and Fr or maximum barrier deflection, with inflection points due to the transitions from trapezoid- to triangle-shaped dead zones. Our findings quantitatively elucidate how flow materials (wet versus dry) and impact dynamics (slow versus fast) control the patterns of the identified bi-linear correlations. This work offers a physics-based reference and insights for improving widely-used impact solutions for geophysical flows against flexible barriers.

1 Introduction

Flexible barriers are increasingly used to mitigate debris flows, debris/rock/snow avalanches, and rockfalls [1-3]. Determining the impact load exerted on a flexible barrier is a fundamental issue in hazard mitigation. Still, it has not been directly measurable in experiments or fields over the past three decades [4-6]. The difficulty is rooted in capturing the multiphase, multiway flow-barrier interactions, where many mechanisms can work simultaneously. Understanding such impact is thus of deep engineering and scientific importance.

The impact loads of geophysical flows on flexible barriers are typically estimated by simplified [2, 3, 7] and Froude-number-related analytical [8, 9] solutions. Nonetheless, impact loads estimated by simplified solutions in physical tests lack scrutiny but are frequently referred to as reliable data for calibrating Fr-related analytical solutions [8, 9]. Alternatively, many numerical methods, including continuum-based [10], discrete-based [11] and coupled frameworks [12, 13], have been developed to explore the impacts on flexible barriers by geophysical flows. However, simplifications of the solid-liquid flow dynamics [10, 11] and 3D nonuniform, permeable flexible barriers [12, 13] have prevented a deeper understanding of the underlying relations and mechanisms behind the flow-barrier interactions.

Towards a unified description of the impacts when geophysical flows of variable natures against a flexible barrier system, this study scrutinizes underlying relations and mechanisms for widely-used solutions based on direct, numerical measures of flow-barrier forces and barrier load-deflection relations.

2 Methods and model setup

A coupled computational fluid dynamics and discrete element (CFD-DEM) method is employed to probe the dynamics during geophysical flows against a flexible barrier. A flexible barrier is modeled by DEM (Fig. 1a), while a debris flow is simulated as a mixture of discrete particles and a continuous slurry by DEM and CFD (Fig. 1d), respectively. A two-way coupling scheme offers a unified way to describe the solid-liquid interactions in a debris flow and between barrier components and debris liquid. The motions of a particle are governed by Newton's equations, and the fluid is controlled by the locally-averaged Navier-Stokes equation for each fluid cell with the finite-volume method. Further details can be found in our previous work [8, 14]. This method has been benchmarked with classic geomechanics problems [14] and various engineering conditions [13, 15, 16, 17].

2.1 Modeling a flexible ring net barrier

A flexible barrier typically consists of a ring net, brake elements, and cables (Fig. 1a-upper). It is modeled by assembling the main ring net, ten brake elements, and five supporting cables (Fig. 1a-lower). The bottom and lateral edges of the top and middle cables are fixed, mimicking the anchored boundaries. The Parallel Bond Model [18] implemented in DEM is employed to model all barrier components as connected nodal particles. For example, interlocking rings are idealized as connected nodal particles (Fig. 1b). Fig. 1c displays the local deformations of cable-ring-ring connections, consistent with field observations [3].

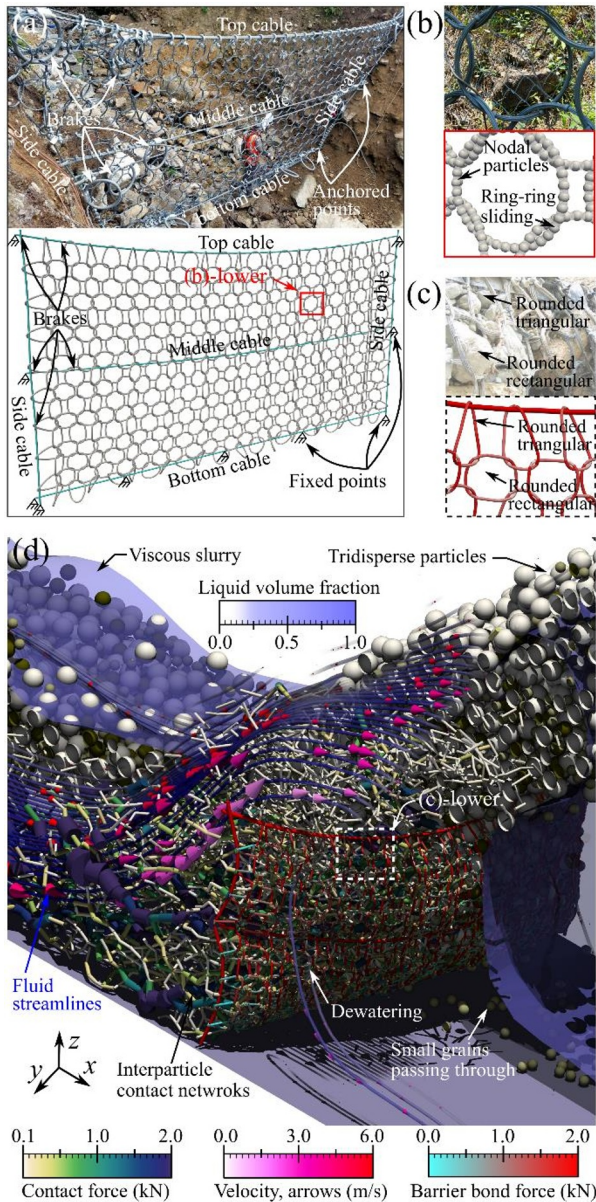* Corresponding author: mfguan@hku.hk

Fig. 1. Model setup and a typical impact scenario. (a), (b) and (c) present a comparison between field photos and numerical snapshots for the barrier, interlocking rings and local deformation characteristics, respectively. (d) shows a debris flow impacting the barrier, where split views display debris fluid and gap-graded particles (back half-space) as well as fluid streamlines and interparticle contacts (front half-space).

2.2 Model setup and simulated dynamics

We perform systematic simulations of Debris Flows (DF), Debris Avalanches (DA) and Rock Avalanches (RA) impacting a flexible barrier. A broad range of Fr $(0.5 \sim 8.7)$ is produced with a pre-impact flow depth of ~ 0.3 m and varying initial velocities $v_{int} = 0.5$ m/s ~ 14 m/s. Fig. 1d shows a typical debris flow impacting a reduced-scale flexible barrier (0.9m-high, 1.8m-wide) constructed on an inclined channel with a slope of 20°, capturing critical physical processes, such as flow climbing, silting and retaining, the cable-ring-ring sliding, dewatering and small particles passing through.

Details of model geometry, debris-flow materials, barrier models and simulation conditions can be found in our newly published paper [8], which has complied a

unified design diagram for flexible, slit and rigid barriers. By contrast, this work focuses on elucidating how flow materials and dynamics affect underlying relations for impacts of geophysical flows on a flexible barrier. Herein, the initial heights of viscous slurries in DF, DA and RA cases are set to 0.3 m, 0.15 m and 0 m, respectively. Clear differences in flow redirection, separation and overtopping dynamics, and barrier responses among DF, DA and RA cases can be observed from Videos S1, S2 and S3 that can be permanently archived at https://doi.org/10.5281/zenodo.6779488.

3 Results and discussion

3.1 Flow-barrier interactions and forces

Figs. 2a, 2b and 2c compare three key flow-barrier interactions for debris flows against flexible barriers observed between a large-scale flume test [6] with a reduced-scale flexible ring net barrier (0.6m-high, 2m-wide) and a DF case under Fr similarity. The numerical predictions well capture experimental observations on the deformed barrier at stages *II*, a certain volume of the fluid and small particles passing through the barrier at stages *II* and *III*, and the curved flow path at stage *III*.
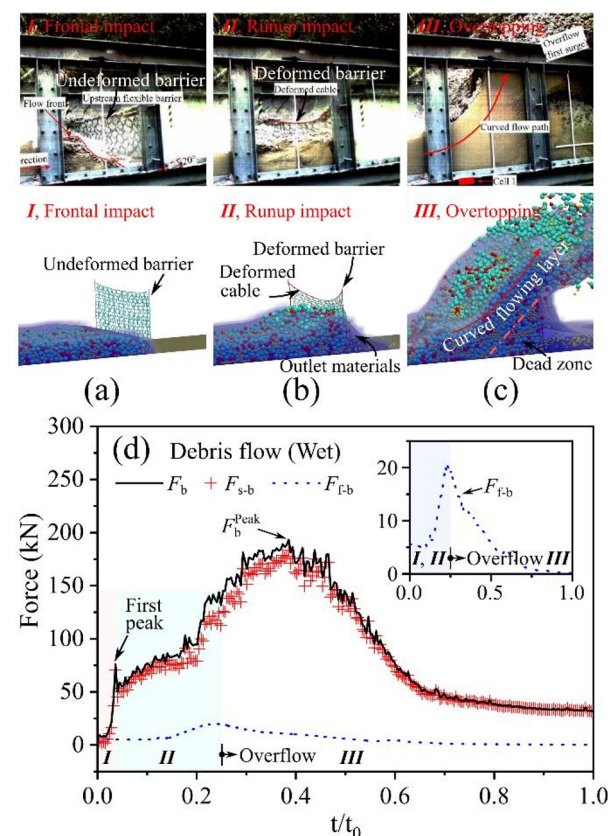

Fig. 2. Comparisons between experimental observations [1] and a representative DF case ($v_{int} = 6$m/s) on key flow-barrier interactions: (a) frontal impact, (b) runup and (c) overflow. (d) presents temporal evolutions of flow-barrier forces in this DF case.

Further, both the in-flow solid and fluid can exert loads on a barrier, including solid-barrier contact force F_{s-b} and fluid-barrier interaction force F_{f-b}, resulting in

the total impact load F_b. This enables direct measure that delineates load components to F_b from individual debris-flow phases. Fig. 2d indicates that the peak value of the fluctuating solid-barrier contact forces (183.2 kN) is around nine times larger than that of the smooth fluid-barrier interaction forces (20.3 kN, see inset in Fig. 2d). Thus, F_{s-b} is the dominant debris-flow load contributor on a flexible barrier. Moreover, solid particles also trigger the first peak during the frontal impact (Fig. 2d), wherein the peak barrier load commonly occurs for rigid countermeasures [2, 8]. In contrast, F_b^{Peak} appears during overtopping for a flexible barrier (Fig. 2d), wherein flowing layer coexists with dead zones [16, 19] (Fig. 2c). Therefore, F_b^{Peak} should be calculated as the sum of loads from the flowing layer and dead zone, especially in designing multi-level flexible barriers.
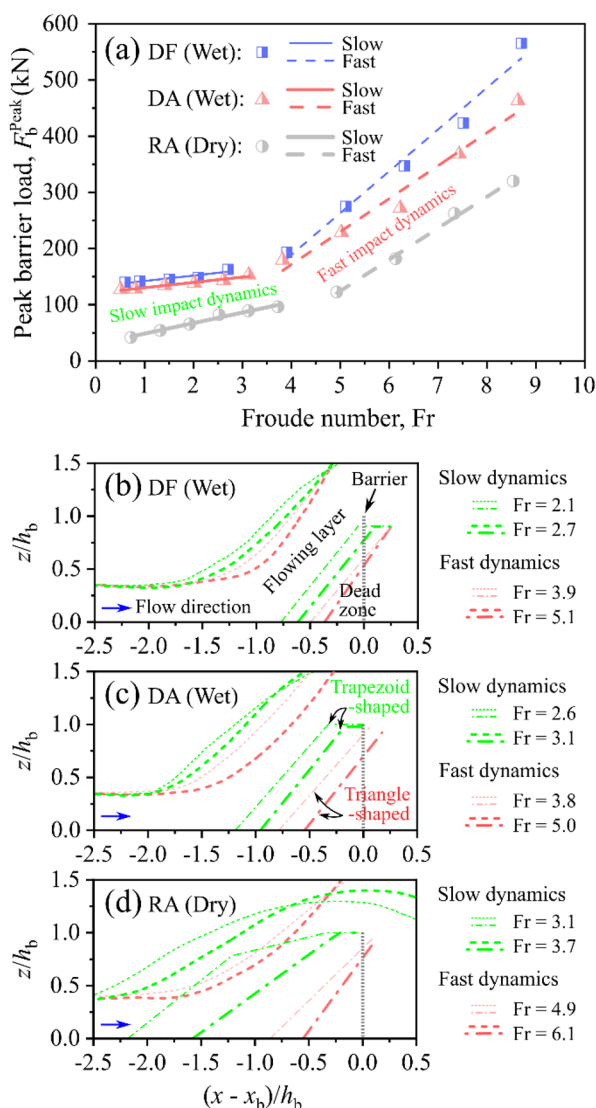

Fig. 3. A unified diagram (a) show how flow types and impact dynamics affect Fr-F_b^{Peak} relations. (b), (c) and (d) display free surfaces of flowing layers (dash lines) and boundaries of dead zones (dash-dotted lines) measured at peak impacts for DF, DA and RA cases near the slow-to-fast transitions in (a), respectively. h_b and x_b denote the height and x-axis location of the barrier, respectively.

Fig. 3a witness the bi-linear, positive Fr-F_b^{Peak} relations that underpin widely-used Fr-related analytical

solutions [8,9,15], with inflection points due to the shifts from trapezoid- to triangle-shaped dead zones (Figs. 3b ~ 3d). The boundaries of dead zones (runup surfaces) are roughly determined according to a velocity threshold [19], and details are presented in supplementary Fig. S1 (https://doi.org/10.5281/zenodo.6779488). We refer the shifts of dead zones to identify the slow-to-fast transitions of flow impact dynamics, which occurs at a higher Fr with a larger solid fraction of impinging flows. Further, the slope of Fr-F_b^{Peak} relations in DF cases under fast impact dynamics is 7.7 times that under slow impact dynamics, whilst this ratio is around 3 for RA cases. Dry flows undergo a smaller bulk density and a longer energy-dissipative runup surface than wet flows (Figs. 3b and 3d). Further, grain shear stress is considered more effective in energy dissipation than fluid viscous shearing [20], and the viscous slurry may enhance flow velocity and impact pressures by decreasing the inter-particle friction [21] and dampening particle collisions [22]. Our results highlight that the discriminants of flow types (DF, DA or RA) and impact dynamics (slow or fast) are crucial for predicting Fr-F_b^{Peak} relations, thereby enable potential improvements of the Fr-related analytical solutions.

3.2 Barrier load-deflection relations

Understanding barrier load-deflection phenomena is vital for evaluating peak impact, barrier deformation, and retainment capacity for practical designs. Notably, the spring solution given by $F_b = k_b^n D_h$ are investigated in the estimates of impact loads [3,7], where k_b^n and D_h represent the equivalent barrier stiffness and maximum barrier deflection in the flow direction. We also present the complex F_b-D_h relations in supplementary Fig. S2 (https://doi.org/10.5281/zenodo.6779488).
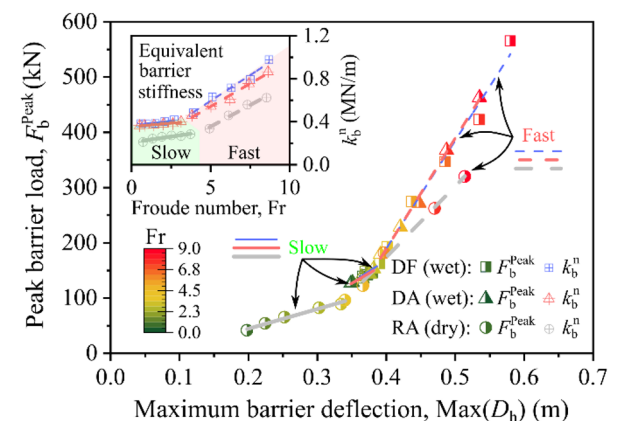

Fig. 4. A diagram showing the effects of flow materials and impact dynamics on Max(D_h)-F_b^{Peak} and Fr-k_b^n relations. The slow-to-fast transitions are consistent with Fig. 3.

Fig. 4 presents the influences of flow types and impact dynamics on Max(D_h)-F_b^{Peak} relations, revealing the bi-linear, positive correlations. Max(D_h) and F_b^{Peak} are crucial designing factors and positively correlated with Fr. Further, fast impact dynamics witness a higher slope of Max(D_h)-F_b^{Peak} relations than slow impact dynamics. Because trapezoid-shaped dead zones (slow)

undergo longer energy-dissipative runup surface and larger volume of trapped debris than the triangle-shaped ones (fast, Figs. 3b ~ 3d). The slope of $\text{Max}(D_h)$-F_b^{Peak} relation in dry cases under either slow or fast impact dynamics is around half that in wet cases, owing to higher energy-sinking efficiencies of flowing layer and dead zone in dry flows. For DF and DA cases, similar trends of $\text{Max}(D_h)$-F_b^{Peak} relations are observed, while the magnitudes of $\text{Max}(D_h)$ and F_b^{Peak} in DA cases are smaller than in DF cases under similar Fr. These results indicate that flow materials (wet or dry) primarily control the trend of $\text{Max}(D_h)$-F_b^{Peak} relations, while a larger bulk density in a wet flow produces more significant $\text{Max}(D_h)$ and F_b^{Peak} under similar Fr.

The inset in Fig. 4 also witnesses the bi-linear, positive correlations between Fr and k_b^n. Under fast impact dynamics, k_b^n increases rapidly with increasing Fr in all cases, wherein RA (dry) cases present the minimum slope. It indicates that k_b^n changes with flow materials and Fr conditions under fast impact dynamics, regardless of the same barrier. Under slow impact dynamics, k_b^n is roughly constant in either dry (RA: ~ 0.26 MN/m) or wet cases (DF: ~ 0.39 MN/m; DA: ~ 0.38 MN/m). Thus, the hypothesis of constant k_b^n in spring solution is justified under slow impact dynamics, whereas its rationality is not guaranteed under fast impact dynamics or with different impinging flows.

4 Conclusions

This work presents systematic simulations of a flexible barrier system against geophysical flows of variable natures to identify underlying relations and mechanisms of the multiphase, multiway interactions. The employed fluid-solid coupling model captures essential physics observed in experiments and fields.

Physics-based numerical measures of flow-barrier forces and barrier load-deformation behaviors reveal the bi-linear, positive relations underpinning widely-used impact solutions, with inflection points caused by the transitions from trapezoid- to triangle-shaped dead zones. Specifically, the identified correlations relate the peak impact load to Froude-number or maximum barrier deformation. Our findings facilitate determining the impact loads of geophysical flows on flexible barriers based on flow materials (wet versus dry) and impact dynamics (slow versus fast).

Future work may explore the existence of similar relationships regarding the complexity of geophysical flows, including huge boulders [1], varying flow heights [3], and erosion [23].

References

1. R. M. Iverson, Rev. Geophys. **35(3)**, 245-296 (1997) doi: 10.1029/97RG00426

2. C. W. Ng, D. Song, C. E. Choi, L. H. D. Liu, J. S. Kwan, R. C. H. Koo, W. K. Pun, Can. Geotech. J. **54(2)**, 188-206 (2017) doi: 10.1139/cgj-2016-0128

3. C. Wendeler, *Debris-flow protection systems for mountain torrents*. WSL. (2016)

4. J. S. DeNatale, R. M. Iverson, J. J. Major, R. G. LaHusen, G. L. Fiegel, J. D. Duffy, Open-File Rep. 99-205 (1999) doi: 10.3133/OFR99205.

5. L. Bugnion, B. W. McArdell, P. Bartelt, C. Wendeler, Landslides **9(2)**,179-187 (2012) doi: 10.1007/s10346-011-0294-4.

6. H. Vicari, C. W. Ng, S. Nordal, V. Thakur, W. R. K. De Silva, H. Liu, C. E. Choi, Can. Geotech. J. **59(6)** (2022) doi: 10.1139/cgj-2021-0119

7. W. Ashwood, O. Hungr, Can. Geotech. J. **53(10)**, 1700-1717 (2016) doi: 10.1139/cgj-2015-0481

8. Y. Kong, M. Guan, X. Li, J. Zhao, H. Yan, J. Geophys. Res. Earth. Surf. **127(6)** (2022) doi: 10.1029/2021JF006587

9. D. Song, Zhou, X. Q. Chen, X. Q. J. Li, A. Wang, P. Peng, K. X. Xue, Eng. Geol. **288** (2021) doi: 10.1016/j.enggeo.2021.106154

10. L. Zhao, J. W. He, Z. X. Yu, Y. P. Liu, Z. H. Zhou, S. L. Chan, Landslides **17(12)**, 2723-2736 (2020) doi: 10.1007/s10346-020-01463-x

11. A. Albaba, S. Lambert, F. Kneib, B. Chareyre, F. Nicot, Rock Mech. Rock Eng. **50(11)**, 3029-3048 (2017) doi:10.1007/s00603-017-1286-z

12. A. Leonardi, F. K. Wittel, M. Mendoza, R. Vetter, H. J. Herrmann, Comput-Aided Civ. Inf. **31(5)**, 323-333 (2016) doi: 10.1111/mice.12165

13. Y. Kong, X. Li, J. Zhao, Eng. Geol. **289**, 335-349 (2021) doi: 10.1016/j.enggeo.2021.106188

14. J. Zhao, T. Shan, Powder Technol. **239**, 248-258 (2013) doi: 10.1016/j.powtec.2013.02.003

15. X. Li, J. Zhao, K. Soga, Géotechnique **71(8)**, 674-685 (2021) doi: 10.1680/jgeot.18.P.365

16. Y. Kong, J. Zhao, X. Li, Powder Technol. **386**, 335-349 (2021) doi:10.1016/j.powtec.2021.03.053

17. X. Li, J. Zhao, J. S. Kwan, Comput. Geotech. **128** (2020) doi: 10.1016/j.compgeo.2020.103850

18. D. O. Potyondy, P. A. Cundall, Int. J. Rock Mech. Min. Sci. **41(8)**, 1329-1364 (2004) doi: 10.1016/j.ijrmms.2004.09.011

19. T. Faug, R. Beguin, B. Chanut, Phys. Rev. E **80(2)** (2009) doi: 10.1103/PhysRevE.80.021305

20. J. Fang, L. Wang, Y. Hong, J. Zhao, Géotechnique **72(5)**, 391-406 (2022) doi: 10.1680/jgeot.19.P.160

21. H., Zheng, Z., Shi, T., de Haas, D., Shen, K. J., Hanley, B. Li, J. Geophys. Res. Earth. Surf. **127(3)** (2022) doi: 10.1029/2021JF006488

22. R. Kaitna, M. C. Palucis, B. Yohannes, K. M. Hill, W. E. Dietrich, J. Geophys. Res. Earth. Surf. **121(2)** (2016) doi: 10.1002/2015JF003725

23. R. M. Iverson, M. E. Reid, M. Logan, R. G. LaHusen, J. W. Godt, J. P. Griswold, Nat. Geosci. **4(2)**, 116-121 (2011) doi: 10.1038/ngeo1040